

## BIOMECHANICS

# Jumping on water: Surface tension-dominated jumping of water striders and robotic insects

Je-Sung Koh,<sup>1,2\*</sup> Eunjin Yang,<sup>3\*</sup> Gwang-Pil Jung,<sup>1</sup> Sun-Pill Jung,<sup>1</sup> Jae Hak Son,<sup>4</sup> Sang-Im Lee,<sup>4,5</sup> Piotr G. Jablonski,<sup>4,6</sup> Robert J. Wood,<sup>2</sup> Ho-Young Kim,<sup>3,5†</sup> Kyu-Jin Cho<sup>1,5†</sup>

Jumping on water is a unique locomotion mode found in semi-aquatic arthropods, such as water striders. To reproduce this feat in a surface tension-dominated jumping robot, we elucidated the hydrodynamics involved and applied them to develop a bio-inspired impulsive mechanism that maximizes momentum transfer to water. We found that water striders rotate the curved tips of their legs inward at a relatively low descending velocity with a force just below that required to break the water surface (144 millinewtons/meter). We built a 68-milligram at-scale jumping robotic insect and verified that it jumps on water with maximum momentum transfer. The results suggest an understanding of the hydrodynamic phenomena used by semi-aquatic arthropods during water jumping and prescribe a method for reproducing these capabilities in artificial systems.

**W**ater striders skate easily on the surface of water mainly because their low body mass and superhydrophobic legs allow them to be supported on their tarsi (the proximal segment of an arthropod's foot) by surface tension alone (1–3). They are able to generate sufficient vertical propulsion to disengage or jump from the water surface—actions that require high momentum with a high vertical take-off velocity.

Previous studies of the mechanics of water-“walking” in a variety of animals, from small insects to reptiles, elucidated the mode of momentum transfer to the water (1–6): The velocity of the driving leg was found to play a dominant role. Comparatively heavy animals with a high Baudoin number [ $Ba = Mg/(\sigma P) \gg 1$ , where  $M$  is the mass,  $g$  is the gravitational acceleration,  $\sigma = 72 \text{ mN m}^{-1}$  is the surface tension of water at 25°C, and  $P$  is the contact perimeter] cannot float on the surface, so they commonly use high driving power and speed to generate inertial forces in the water large enough to support their weight. For example, the basilisk lizard paddles its foot downward to expand an air cavity under the water and then pulls its foot out of the water before the cavity

collapses (7). Limb strokes at velocities higher than  $30 \text{ ms}^{-1}$  induce large hydrodynamic forces, including viscous drag and inertia from the water. In contrast, small arthropods covered with water-repellent integuments (a skin of the arthropod) can float on water without effort because of surface tension ( $Ba < 1$ ). Hu *et al.* (1, 4), Denny (5, 8), and Suter *et al.* (3) have reported plausible propulsion mechanisms for small water surface-dwelling animals. These animals achieve horizontal momentum transfer by generating a capillary wave on the water surface and vortices beneath the surface.

Although several small-scale robots inspired by the water strider have demonstrated the ability to float and locomote on water by partly or fully using surface tension (4, 9, 10), none of them jumps on water. Furthermore, jumping that involves interactions between the unconstrained free body and the liquid surface has been poorly understood at the scale of insects (11, 12). Jumping is vertical propulsion, and it requires different criteria from walking on water, which is lateral propulsion. In contrast to jumping on solid ground, a large driving force and fast stroke in the jumping leg do not guarantee a high take-off velocity on the water surface, especially for small insects (11, 12). There are small insects, such as pygmy mole crickets, that still manage to jump on water by taking advantage of viscosity via a high driving acceleration and leg velocity ( $>130,000 \text{ s}^{-1}$ ). But their water-jumping performance is much lower than when they jump on solid ground (13).

Water striders can jump on water as high as they can jump on land (1). When they are exposed to danger, they show extremely high jumping performance and land in an uncontrolled manner. We focused on this extreme case that achieves the maximum momentum transfer on water. To

explore this amazing semi-aquatic motility, we collected water striders (*Aquarius paludum*) from a local pond and recorded them jumping on water in the laboratory with high-speed cameras (Fig. 1A and materials and methods section 1). We found that their ability to exploit the water surface comes from maximizing momentum transfer to the body, which is the integration of force with respect to time by Newton's second law of motion. That is, the water strider gradually increases its leg force to the limit allowed by the water surface and maintains that force until it disengages from the water surface.

High-speed imaging experiments revealed that the insect rises upward while pushing the water surface downward and closing four of its legs inward (Fig. 1A). The hydrodynamic forces generated during this leg motion include drag, surface tension, buoyancy, inertia, and viscous friction. On the basis of estimates of each force using representative values of parameters for the insects we observed (tables S4 and S5), we found that the surface tension force dominates the other forces (supplementary text section 2) for the Weber number,  $We = \rho U^2 D / \sigma \sim 10^{-2}$ , and  $Ba = Mg/(\sigma P) \sim 10^{-2}$ . Here,  $\rho$  is the density of water,  $U \sim 0.2 \text{ m s}^{-1}$  is the rate of dimple growth (i.e., the depression resulting from the force imparted by the leg),  $D \sim 0.1 \text{ mm}$  is the leg diameter,  $M \sim 40 \text{ mg}$  is the mass of the insect, and  $P \sim 80 \text{ mm}$  is the perimeter of the legs that defines the contact length. The low value for  $We$ , because of the slow stroke with a thin leg, implies a small energy loss through water flow compared with the interfacial energy of the curved water surface. This inertia-free interaction between the legs and the water surface ensures that the legs remain in contact with the water surface during the down stroke, thereby fully exploiting the reaction force of the curved meniscus on the legs. If the legs struck the water at high speed, the water surface would retreat fast enough to lose contact with the legs and splashing would ensue, decreasing the efficiency of momentum transfer between the legs and water surface (12). The combination of a light body with a long perimeter (low  $Ba$ ) indicates an ability to generate an extremely high body acceleration (compared with  $g$ ) by using the surface tension of water. Consequently, low  $We$  and  $Ba$  collectively contribute to the high acceleration of a jumping body through surface tension-dominated interaction without notable energy loss to the water.

A small  $We$ , implying negligibly small dynamic effect on the interaction between the legs and the meniscus (14), allows the use of static calculations of interfacial force based on the depth of the meniscus (see supplementary text section 2 and table S1). Because the surface tension force on a floating wire tends to increase with the depth of the dimple (figs. S10 to S12) (15), it is desirable to push the water surface as deeply as possible. However, the meniscus ruptures when the leg descends beyond the depth limit that the surface tension of water can endure, leading to a dramatic reduction of the reaction force on the

<sup>1</sup>Biorobotics Laboratory, Department of Mechanical and Aerospace Engineering, Seoul National University, Seoul 151-744, Korea. <sup>2</sup>School of Engineering and Applied Sciences and Wyss Institute for Biologically Inspired Engineering, Harvard University, Cambridge, MA 02138, USA. <sup>3</sup>Micro Fluid Mechanics Laboratory, Department of Mechanical and Aerospace Engineering, Seoul National University, Seoul 151-744, Korea. <sup>4</sup>Laboratory of Behavioral Ecology and Evolution, School of Biological Sciences, Seoul National University, Seoul 151-742, Korea. <sup>5</sup>Institute of Advanced Machines and Design, Seoul National University, Seoul 151-744, Korea. <sup>6</sup>Museum and Institute of Zoology, Polish Academy of Sciences, Warsaw 00-679, Poland.

\*These authors contributed equally to this work.

†Corresponding author. E-mail: hyk@snu.ac.kr (H.-Y.K.); kjcho@snu.ac.kr (K.-J.C.)

jumping body (16). A superhydrophobic straight cylinder of negligible diameter lying horizontally on a water surface can depress the interface roughly by the capillary length (17) without sinking. The load supported by a floating object is equal to the weight of water displaced by the body and the perturbed free surface (18). It has already been suggested that adaptive deformation of joints and the flexibility of the tibia and tarsus of the water strider's leg may prevent the tip of the leg from piercing the water meniscus and increase the supporting force of the water surface by increasing the water volume displaced (19). Figure 1B shows that the tapered leg keeps its tip pointing upward during the stroke, helping to prevent rupture of the meniscus. By using a theoretical model to deduce the force acting on a flexible cylinder floating on liquid (with two parallel contact lines along its axis), we found that the maximum force per unit length ( $f$ ) on the legs of the water striders is always close to but below a value corresponding to twice the surface tension of water,  $144 \text{ mN m}^{-1}$ , which is the maximum value that water surface can withstand (Fig. 1C, supplementary text section 2, and table S1).

Careful observation of the jumping sequence of the water strider (Fig. 1A) reveals that the insect rotates its middle and hind legs rather than merely pushing them downward. That is, legs that are initially sprawled on the water surface are extended downward at take-off through actuated leg rotation. To explain the mechanical advantages of this leg movement, we consider what would happen if the leg morphology and kinematics were such that the water strider could depress the surface only vertically without rotation. Upon reaching the maximum dimple depth,  $l_c$ , the meniscus is recovered at a velocity of  $U \sim l_c/t_r \sim 10^{-1} \text{ m s}^{-1}$ , where  $t_r$  is the time scale for the capillary-gravity wave to travel the capillary length (20, 21). This is far lower than the take-off velocity of the real water strider,  $V \sim 1 \text{ m s}^{-1}$ , as evidenced by the relatively slower recovery of the meniscus (from 0 to 14 ms in Fig. 1A) compared with fast disengagement of the legs from the water surface. This implies that the fast-rising water strider would be able to use the upward force from the meniscus only while the legs contact and depress the water surface, thereby significantly reducing the time for momentum transfer. In reality, however, the water strider rotates its legs during jumping, which ensures that the legs meet an undistorted water surface continuously. Thus, the legs can keep pressing the water surface to the maximum depth during ascent of the body despite the slow recovery speed of the meniscus. Our observation reveals that the extended time of interaction between the water surface and the rotating legs of the four water striders tested leads to an increase of  $V$  of 27% to 42% as compared with the case when the legs are assumed to move only vertically. Therefore, water striders maximize momentum transfer to the water surface by maintaining a high force profile on each leg until the last moment of jumping by depressing the water

surface to the capillary length while rotating their legs.

On the basis of our understanding of real water striders, we identified design criteria for our at-scale robot. Superhydrophobic legs and a low body mass compared with surface tension, yielding  $Ba \ll 1$ , are conducive to higher acceleration with maximum use of surface tension force. In addition, to maximize the kinetic energy transfer to the robot instead of the water, locomotion with low descent velocity and thin legs ( $We \ll 1$ ) are required. The driving force should be gradually increased to the maximum value of  $144 \text{ mN m}^{-1}$  ( $2\sigma$ ) to prevent the robot's legs from penetrating the water surface during a jump. If the water surface is broken, the legs swing rapidly under the water surface, leading to high levels of splash

and flow around the legs that dissipate energy, rendering jumping highly inefficient (Fig. 2). These criteria guarantee surface tension–dominant propulsion with minimal energy dissipation to water flow.

An ultralight impulsive system that can maximize momentum transfer with limited maximum driving force is required. Leg rotation is also required to ensure that the legs continuously meet an undistorted water surface and keep pressing the water surface. The leg shape should be designed to maximize the surface tension force in the same way as the flexible legs of water striders adapt to the dimple. Especially, the shape of the tip is strongly related to the wetted length when the legs of the water strider rotate inward (17). Therefore, the leg tip should be curved in order to

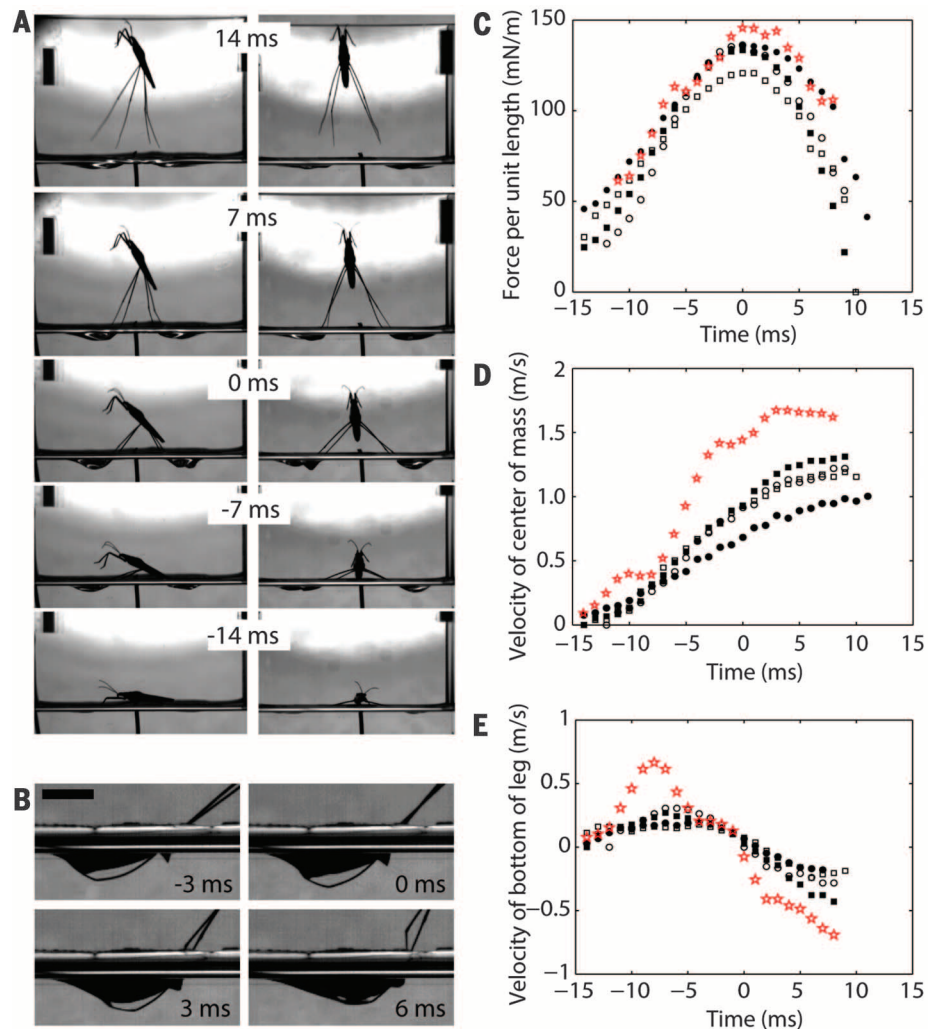


**Fig. 1. Water strider jumping.** (A) Jumping sequence of a water strider in side view (left column) and front view (right column). The black bars on the walls are 10-mm-long scale bars. See movie S5. (B) Bent leg of a water strider pushing the water surface. The wetted part of the leg moves to the right, resulting in meeting an undistorted water surface continuously. The scale bar indicates 5 mm. (C)  $f$  on the four legs of four water striders and robot 4. (D) Velocity profile of the water striders and robot 4 jumping from water. (E) Velocity profile of the bottom of the leg for water striders and robot 4. (C to E) Black symbols indicate four different water striders, and red stars indicate robot 4. The time is set to be zero when the maximum force is generated. See tables S1 and S3 for detail descriptions of the water striders and the robot.

adapt to the dimple with increasing wetted length while the legs rotate. The low  $We$  constraint can be rewritten as  $t \gg (\rho h^2 D / \sigma)^{1/2}$  by using  $U \sim h/t$ , where  $h$  is the maximum dimple depth and  $t$  is the interaction time with water, which results in  $t \gg 10^{-3}$  s for both real water striders and our at-scale robot (tables S1 to S4).

The robot uses a bio-inspired catapult mechanism adapted from a flea (22, 23) and implemented with flexure hinge-based composite structures (24). The torque reversal catapult (TRC) mechanism in the flea's jumping leg is capable of rapid and repeatable torque production without complex mechanisms. It generates a very small torque when initially triggered, and the torque gradually increases through the driving stroke, as shown in Fig. 3G. This torque profile results in high momentum transfer from the water surface to the jumping body. In contrast, a high initial torque

would create a large splash and waves on the water surface. Gradually increasing the torque minimizes unnecessary energy transfer to the water, allowing the jumping body to obtain maximum momentum.

The catapult mechanism uses composite materials and planar shape memory alloy (SMA) actuators. A similar TRC mechanism was previously developed to build a small-scale ground-jumping robot (22, 23). The driving forces for our jumping robot can be varied by changing actuator stiffness and leg length. The passive trigger, which is the compliant beam component that holds the actuator, determines the required force for triggering the geometrical latch of the TRC and the stiffness of the actuator at the moment of triggering (fig. S6). This automatic triggering mechanism simplifies the latch system of the robot and makes it possible to minimize the size and

weight of the structure. The 68-mg body weight is 6% of the maximum surface tension force that water can support (on legs with a 160-mm-long perimeter), corresponding to a  $Ba$  of 0.06, much less than 1 (table. S5). Theoretically, the robotic water strider can be vertically accelerated by a surface tension force up to 15 g. In jumping experiments, the robot achieved 13.8 g, which is close to the maximum acceleration.

When the legs swing, the length of the leg influences the reaction force on the legs primarily because it determines the moment arm of the driving legs, which transfers the torque generated by the TRC mechanism into a vertical reaction force. In nature, one long-legged water-jumping arthropod was shown to have driving legs 170% longer than its body (16). To reduce the maximum reaction force below the maximum surface tension force, we made the robot's legs 5 cm, longer than those of a water strider, because of the higher torque capabilities of the robot.

The pop-up book microelectromechanical system (MEMS) fabrication process (24–28) allowed us to build at-scale prototypes just 2 cm in body length and 68 mg in weight (Fig. 3D). This fabrication process avoids complex assembly steps by leveraging self-assembly techniques inspired by the folded components of pop-up books. This paradigm for fabricating micro- and “meso”-scale robots (22–28) is based on flexure hinge-based folded composites. The process involves layering and laminating sheets of individual materials, then folding the composite into a three-dimensional structure (fig. S5). The flexure hinges eliminate

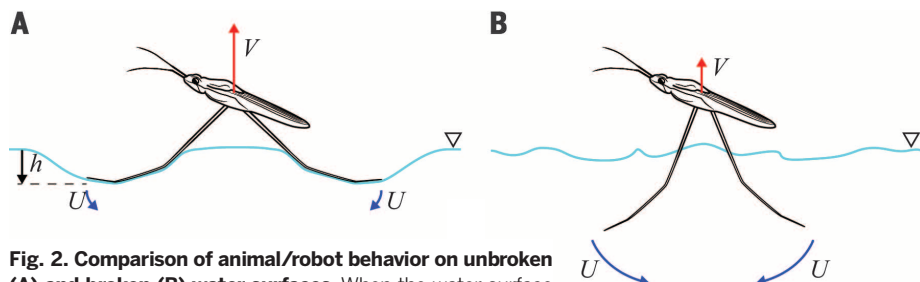
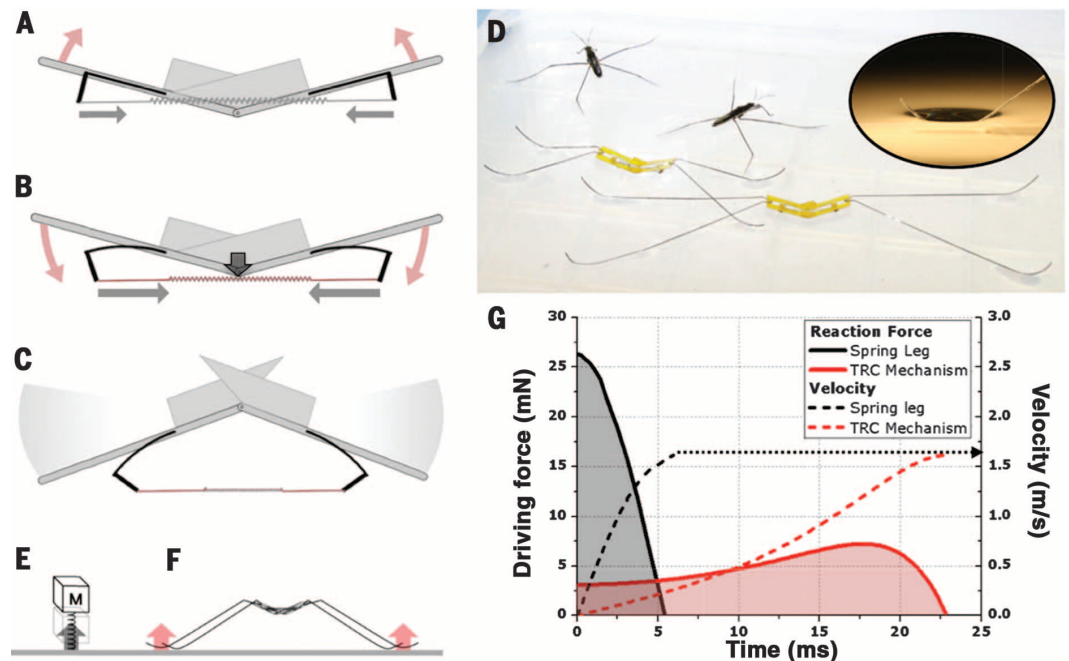


**Fig. 2. Comparison of animal/robot behavior on unbroken (A) and broken (B) water surfaces.** When the water surface is broken ( $f > 2\sigma$ ), the force supporting the legs sharply reduces, causing the legs to swing rapidly into the water. The resulting viscous drag and splashing dissipate energy.

**Fig. 3. The TRC mechanism inspired by a flea's jumping leg.** (A to C) The principle of the mechanism. (A) Initial position. The actuator (shown as a coil) is attached at each compliant L-shaped cantilever. The actuator pulls the structure upward, but stoppers block the movement. (B) The actuator begins bending down the compliant L-shaped cantilever, which also moves the actuator down. (C) When the actuator passes through the center joint (i.e., the singularity of the mechanism), the torque direction is reversed, and the structure swings rapidly. The stored energy in the actuator and the cantilevers is released at once. (D) Two jumping robotic insects with different leg lengths, along with real water striders. The legs are coated with a hydrophobic material, resulting in a high contact angle that creates a dimple (inset image) on the water surface, which supports the weight of the robot. (E and F) Comparison of two jumping mechanisms, compressed spring legs (E) and a TRC mechanism (F). In contrast to the spring leg, a TRC mechanism may reduce the driving force on the legs by its torque characteristics and long length of the legs. (G) The driving force and velocity profiles of compressed spring legs and a TRC mechanism. The TRC mechanism requires much less maximum force to attain the same velocity. In comparison, the stroke of the actuators (springs) in both models is 5.75 mm, and their stiffness is set to generate the same  $V$  of  $1.6 \text{ m s}^{-1}$  ( $4.4 \text{ N m}^{-1}$  in spring leg,  $16.52 \text{ N m}^{-1}$  in TRC mechanism).



(E and F) Comparison of two jumping mechanisms, compressed spring legs (E) and a TRC mechanism (F). In contrast to the spring leg, a TRC mechanism may reduce the driving force on the legs by its torque characteristics and long length of the legs. (G) The driving force and velocity profiles of compressed spring legs and a TRC mechanism. The TRC mechanism requires much less maximum force to attain the same velocity. In comparison, the stroke of the actuators (springs) in both models is 5.75 mm, and their stiffness is set to generate the same  $V$  of  $1.6 \text{ m s}^{-1}$  ( $4.4 \text{ N m}^{-1}$  in spring leg,  $16.52 \text{ N m}^{-1}$  in TRC mechanism).

friction, one of the dominant causes of energy loss and nonlinearity for small devices. The design parameters are determined by analyzing the compliance of the structure for passively triggering the torque reversal mechanism (see supplementary text section 1 and fig. S6) based on a fully dynamic simulation, including the mechanical properties of all the components and the interface forces between the water surface and the robot's legs (see supplementary text section 2 and fig. S13). Furthermore, all modeling steps are verified and supported by individual experiments. With this simple joint element, dynamic modeling and simulations match well with experimental data obtained with physical prototypes (fig. S3).

The sheet nickel titanium (NiTi) SMA actuator is embedded in the body structure as an artificial muscle. The sheet SMA was cut into a serpentine shape by the same ultraviolet laser micromachining system used to construct the body. The actuator is 80  $\mu\text{m}$  thick, 100  $\mu\text{m}$  wide, and 1 mg in weight. When heated above its transition temperature, the actuator's stiffness changes, inducing a negative strain and pulling the passive trigger in the body structure until the torque direction is reversed (Fig. 3, A to C).

The legs are made of superelastic Ni-Ti alloy to prevent them from permanent deformation

during repeated jumping experiments. The high modulus and superelasticity of this wire permits the legs to be thin and flexible. The end tips of the wire legs in the robot (corresponding to the tarsus in the insect) are curved, which minimizes contact shape change between the legs and the water surface when the legs swing and prevents stress concentration at the interface between the tip and the water surface. The round shape of the wire leg linearizes the resulting surface tension force on the water surface as dimple depth increases, according to the experimental and theoretical modeling results shown in figs. S10 and S12. The linear surface tension force profile allowed us to model the hydrodynamic reaction force between the legs and the water as a spring (see supplementary text section 2 and table S6). This model yields simulations that are well matched with our experiments (within 7% error in  $V$ ; see table S2).

The wire legs are coated with a superhydrophobic material, Everdry (Ultratech International Incorporated, Jacksonville, FL) (29). We achieved more than  $150^\circ$  of contact angle with this coating (supplementary text section 5 and fig. S9). Hydrophobicity increases jumping velocity by reducing downward forces when the legs escape from the free surface (21, 30) and by increasing the maximum static load that water can endure

(6, 20, 21, 30, 31). In particular, the superhydrophobic coating on the wire legs would lead to near zero adhesion to the water when they leave the surface (21).

We built five prototype robots that use different triggering forces. The driving force has a linear relationship with the triggering force. We performed jumping experiments with the prototypes on both water and ground (figs. S1 to S4 and table S2). A thin heating wire was carefully placed just below the robot body to activate the SMA actuator. As the SMA actuator transitions, the force increases, and the passive trigger begins to bend (Fig. 3, A to C). When the actuator passes through the center joint, the torque direction changes, and the body structure folds downward, generating a rapid snap-through.

The experiments verified the design criteria that the driving force per wetted length ( $f$ ) should be below the maximum surface tension force per wetted length ( $2\sigma$ ) in order for the robot to efficiently jump on water with maximum momentum transfer. Figure 4 shows that the robot jumps off the water surface smoothly without breaking the free surface and without making a large splash.  $V$  is  $1.6 \text{ m s}^{-1}$ , with a jumping height of 142 mm, and the maximum reaction force of the dimple is 9.27 mN. When the legs do not penetrate the water surface, the dynamic model

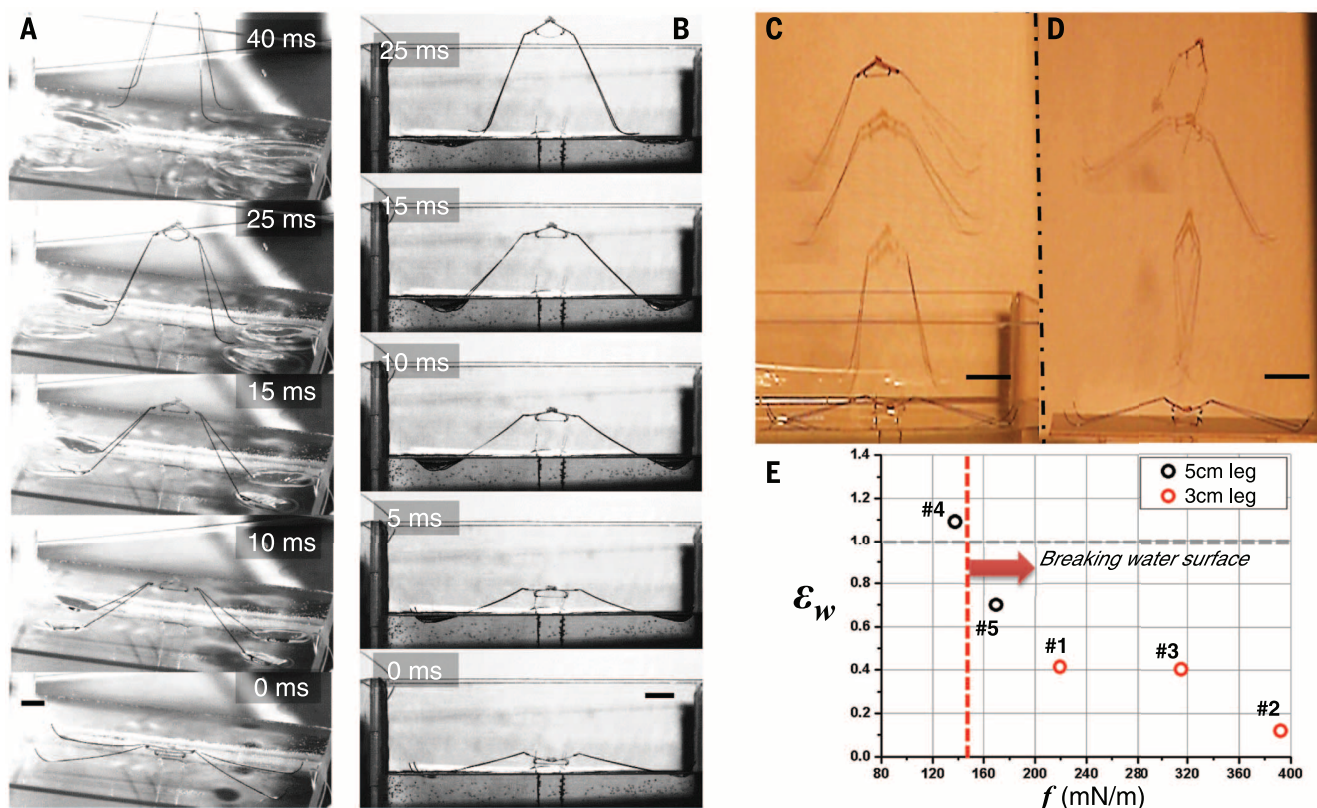


**Fig. 4. Video frames of robot 4 and  $\epsilon_w$  of robots jumping on water and on ground.** (See movies S1 to S4.) (A) The legs distort the water surface. Note the absence of large splashing around the driving legs. (B) These horizontal views show that the legs do not penetrate the water surface. (C) Superimposed frames of the robot jumping on water. (D) Superimposed frames of the robot jumping on rigid ground. The robot obtains similar momentum on water and ground. Scale bar, 1 cm. (E) Experimental results for  $\epsilon_w$  depending on different driving  $f$  of five robot prototypes. The red dashed line indicates the maximum surface tension force that water provides ( $2\sigma$ ,  $144 \text{ mN m}^{-1}$ ). The gray dashed line indicates a  $\epsilon_w$  of 1.

of the robot jumping on water agrees well with experimental data, and we can obtain various reliable simulations from the model (supplementary text section 3 and fig. S3). The maximum driving  $f$  obtained from the dynamic model is  $140 \text{ mN m}^{-1}$ , just below the  $144 \text{ mN m}^{-1}$  ( $2\sigma$ ) limit. Prototypes that satisfied the design criteria achieved higher take-off velocity on water (Fig. 4C) than when jumping on ground (Fig. 4D), a counterintuitive result. This may result from a reduction of leg vibration when jumping on water, because the stored energy is transferred into vertical kinetic energy rather than vibration energy. The movie of these jumps supports this proposition (movie S4). In our models, the initial energy stored in the actuator is  $0.304 \text{ mJ}$  and the jumping kinetic energy of the robot jumping on water is  $0.095 \text{ mJ}$  (31.3%), whereas the vibration kinetic energy is  $0.193 \text{ mJ}$  (63.5%) (table S7).

The water-ground velocity ratio ( $\epsilon_w$ ) describes how much momentum the robot attains on water compared with jumping on solid ground.

$$\text{Water - ground velocity ratio } (\epsilon_w) = \frac{\text{Take - off velocity on water}}{\text{Take - off velocity on ground}}$$

A ratio lower than 1 indicates that the robot did not achieve as much momentum on water as on ground. If the driving force on water is kept below the maximum surface tension force defined by the design criteria, the ratio can be equal to or greater than 1, as was the case for robot 4, which had a maximum driving  $f$  just below the maximum surface tension force ( $2\sigma$ ) (Fig. 4E).  $\epsilon_w$  values of other prototypes are lower than 1, which means that the water surface is broken because of driving force that exceeds this limit, and thus the take-off velocity on water is reduced (table S2 and fig. S3). High driving force does not guarantee a high take-off velocity in a surface tension-dominant case, as shown in robots 1 to 3 and 5. The maximum driving force is constrained by the surface tension coefficient of water. We may assume that water striders control their muscles precisely to satisfy these criteria in a manner similar to the design of the impulsive actuation mechanism in robot 4 (Fig. 1C).

Our at-scale water-jumping robotic insect has demonstrated that it is possible to reproduce the performance of water-jumping arthropods and has proved to be an effective tool for verifying theoretical insights on how the surface tension force can play a dominant role in locomotion of these systems. The experimental results improve our understanding of the dynamic interaction between an unconstrained free body and a liquid surface, as observed in semi-aquatic arthropods in nature.

#### REFERENCES AND NOTES

1. D. L. Hu, J. W. M. Bush, *J. Fluid Mech.* **644**, 5–33 (2010).
2. J. W. M. Bush, D. L. Hu, *Annu. Rev. Fluid Mech.* **38**, 339–369 (2006).
3. R. Suter, O. Rosenberg, S. Loeb, H. Long, *J. Exp. Biol.* **200**, 2523–2538 (1997).
4. D. L. Hu, B. Chan, J. W. M. Bush, *Nature* **424**, 663–666 (2003).
5. M. W. Denny, *Air and Water: The Biology and Physics of Life's Media* (Princeton Univ. Press, Princeton, NJ, 1993).
6. X. Gao, L. Jiang, *Nature* **432**, 36–36 (2004).

7. J. W. Glasheen, T. A. McMahon, *Nature* **380**, 340–342 (1996).
8. M. W. Denny, *J. Exp. Biol.* **207**, 1601–1606 (2004).
9. Y. S. Song, M. Sitti, *IEEE Trans. Robot.* **23**, 578–589 (2007).
10. X. Zhang et al., *ACS Appl. Mater. Interfaces* **3**, 2630–2636 (2011).
11. D.-G. Lee, H.-Y. Kim, *Langmuir* **24**, 142–145 (2008).
12. B. Shin, H.-Y. Kim, K. J. Cho, Towards a biologically inspired small-scale water jumping robot. *2nd IEEE RAS and EMBS International Conference on Biomedical Robotics and Biomechanics* (2008), pp. 127–131.
13. M. Burrows, G. P. Sutton, *Curr. Biol.* **22**, R990–R991 (2012).
14. D. Vella, J. Li, *Phys. Fluids* **22**, 052104 (2010).
15. D. Vella, *Langmuir* **24**, 8701–8706 (2008).
16. M. Burrows, *J. Exp. Biol.* **216**, 1973–1981 (2013).
17. Q.-S. Zheng, Y. Yu, X.-Q. Feng, *J. Adhes. Sci. Technol.* **23**, 493–501 (2009).
18. J. B. Keller, *Phys. Fluids* **10**, 3009 (1998).
19. X.-Y. Ji, J.-W. Wang, X.-Q. Feng, *Phys. Rev. E* **85**, 021607 (2012).
20. D. Vella, D.-G. Lee, H.-Y. Kim, *Langmuir* **22**, 5979–5981 (2006).
21. D.-G. Lee, H.-Y. Kim, *J. Fluid Mech.* **624**, 23 (2009).
22. M. Noh, S.-W. Kim, S. An, J.-S. Koh, K.-J. Cho, *IEEE Trans. Robot.* **28**, 1007–1018 (2012).
23. J.-S. Koh, S.-P. Jung, R. J. Wood, K.-J. Cho, A jumping robotic insect based on a torque reversal catapult mechanism. *2013 IEEE/RSJ International Conference of Intelligent Robots and Systems* (2013), pp. 3796–3801.
24. R. J. Wood, S. Avadhanula, R. Sahai, E. Steltz, R. S. Fearing, *J. Mech. Des.* **130**, 052304 (2008).
25. R. J. Wood, *IEEE Trans. Robot.* **24**, 341–347 (2008).
26. J. P. Whitney, P. S. Sreetharan, K. Y. Ma, R. J. Wood, *J. Micromech. Microeng.* **21**, 115021 (2011).
27. P. Birkmeyer, K. Peterson, R. S. Fearing, DASH: A dynamic 16g hexapedal robot. *2008 IEEE/RSJ International Conference of Intelligent Robots and Systems* (2009), pp. 2683–2689.
28. K. Y. Ma, P. Chirarattananon, S. B. Fuller, R. J. Wood, *Science* **340**, 603–607 (2013).
29. Ultratech International Incorporated, www.spillcontainment.com/everdry.
30. J. Zhao, X. Zhang, N. Chen, Q. Pan, *ACS Appl. Mater. Interfaces* **4**, 3706–3711 (2012).
31. X. Q. Feng, X. Gao, Z. Wu, L. Jiang, Q. S. Zheng, *Langmuir* **23**, 4892–4896 (2007).

#### ACKNOWLEDGMENTS

This work was supported by National Research Foundation of Korea (grant nos. 2013K000371, 2014048162, 2014023206, and 2013R1A2A2A01006394), a grant to Bio-Mimetic Robot Research Center funded by Defense Acquisition Program Administration (grant no. UD130070D), and the Wyss Institute for Biologically Inspired Engineering. We thank H. Choi and B. Shin for their helpful discussions.

#### SUPPLEMENTARY MATERIALS

www.sciencemag.org/content/349/6247/517/suppl/DC1  
Materials and Methods  
Supplementary Text  
Figs. S1 to S13  
Tables S1 to S7  
Movies S1 to S5

20 March 2015; accepted 11 June 2015  
10.1126/science.aab1637

#### PALEOMAGNETISM

## A Hadean to Paleoproterozoic geodynamo recorded by single zircon crystals

John A. Tarduno,<sup>1,2\*</sup> Rory D. Cottrell,<sup>1</sup> William J. Davis,<sup>3</sup> Francis Nimmo,<sup>4</sup> Richard K. Bono<sup>1</sup>

Knowing when the geodynamo started is important for understanding the evolution of the core, the atmosphere, and life on Earth. We report full-vector paleointensity measurements of Archean to Hadean zircons bearing magnetic inclusions from the Jack Hills conglomerate (Western Australia) to reconstruct the early geodynamo history. Data from zircons between 3.3 billion and 4.2 billion years old record magnetic fields varying between 1.0 and 0.12 times recent equatorial field strengths. A Hadean geomagnetic field requires a core-mantle heat flow exceeding the adiabatic value and is suggestive of plate tectonics and/or advective magmatic heat transport. The existence of a terrestrial magnetic field before the Late Heavy Bombardment is supported by terrestrial nitrogen isotopic evidence and implies that early atmospheric evolution on both Earth and Mars was regulated by dynamo behavior.

The oldest previously reported geomagnetic field values, from 3.2 billion- to 3.45 billion-year-old magnetite bearing single feldspar and quartz phenocrysts from igneous rocks of the Nondweni and Barberton Greenstone Belts (Kaapvaal Craton, South Africa) (1–3),

indicate a relatively strong field, but the prior history of the geodynamo is unknown. Some thermal evolution models predict no geodynamo before ~3.5 billion years ago (Ga) (4).

For magnetic minerals to be suitable recorders, they must be small, in the single to pseudosingle domain state (5), and have remained pristine since formation. The metamorphism that has affected Paleoproterozoic and older rocks makes paleointensity determination especially difficult. These metamorphosed rocks typically contain large multidomain magnetic grains (MD) with short relaxation times, secondary magnetic remanence carriers, and minerals with a propensity

<sup>1</sup>Department of Earth and Environmental Sciences, University of Rochester, Rochester, NY 14627, USA. <sup>2</sup>Department of Physics and Astronomy, University of Rochester, Rochester, NY 14627, USA. <sup>3</sup>Geological Survey of Canada, Ottawa K1A 0E8, Canada. <sup>4</sup>Department of Earth and Planetary Sciences, University of California, Santa Cruz, CA 95064, USA.

\*Corresponding author. E-mail: john.tarduno@rochester.edu

*This copy is for your personal, non-commercial use only.*

**If you wish to distribute this article to others**, you can order high-quality copies for your colleagues, clients, or customers by [clicking here](#).

**Permission to republish or repurpose articles or portions of articles** can be obtained by following the guidelines [here](#).

**The following resources related to this article are available online at [www.sciencemag.org](http://www.sciencemag.org) (this information is current as of July 30, 2015):**

**Updated information and services**, including high-resolution figures, can be found in the online version of this article at:

<http://www.sciencemag.org/content/349/6247/517.full.html>

**Supporting Online Material** can be found at:

<http://www.sciencemag.org/content/suppl/2015/07/29/349.6247.517.DC1.html>

A list of selected additional articles on the Science Web sites **related to this article** can be found at:

<http://www.sciencemag.org/content/349/6247/517.full.html#related>

This article **cites 26 articles**, 4 of which can be accessed free:

<http://www.sciencemag.org/content/349/6247/517.full.html#ref-list-1>

This article has been **cited by** 1 articles hosted by HighWire Press; see:

<http://www.sciencemag.org/content/349/6247/517.full.html#related-urls>

This article appears in the following **subject collections**:

Biochemistry

<http://www.sciencemag.org/cgi/collection/biochem>

Engineering

<http://www.sciencemag.org/cgi/collection/engineering>